Available online at www.sciencedirect.com
SCIENCE DIRECT®
ELSEVIER
European Journal of Mechanics B/Fluids 21 (2002) 701–720

Near field vortex dynamics in axially forced, co-flowing jets: quantitative description of a low-frequency configuration

Antonio Lecuona, Ulpiano Ruiz-Rivas *, Pedro Rodríguez-Aumente

Departamento de Ingeniería Térmica y de Fluidos, Escuela Politécnica Superior, Universidad Carlos III de Madrid, Spain

Received 29 November 2001; accepted 12 September 2002

Abstract

This work presents an experimental study of the vortex structures that appear in the shear layer of co-flowing water jets subjected to a strong axial forcing. Quantitative, forcing-phase-locked measurements of the velocity in the near field were obtained using two-component Particle Image Velocimetry (PIV). Two-dimensional vorticity, strain and pressure fields were obtained from these data. Also, some information could be obtained about the azimuthal velocity. The data validates a previous [Rodríguez et al., European J. Mech. B. Fluids 20 (5) (2001) 673–698] qualitative description of the near field vortex dynamics in a highly forced flow, based in inviscid mechanisms, that was supported in low *Re* ($Re_D = 440$) experiments. The experiments presented here show the vortex dynamics is similar for higher Reynolds numbers ($Re_D \approx 7000$) and provides quantitative information of the interesting fields. Also, the present work extends the description to low forcing amplitude cases.

Keywords: Vortex dynamic; Forced flow; Co-flowing jets; PIV

1. Introduction

In this paper we addressed the quantitative study of the vortex dynamics mechanisms that occur in the near field of a complex jet flow. The flow consists of two low Mach number co-flowing jets, and the inner jet is subjected to a finite amplitude axial forcing. The development of the mixing layer in this type of flow was studied in Rodríguez et al. [1] for a laminar ($Re_D = 440$), very high forcing case, using mixing layer visualisation. It was shown that the axial forcing produces considerable changes in the near field organisation of the mixing layer formed by the merging of the two co-flowing jets. For sufficiently high forcing amplitudes, three different types of eddies appear in the near field. They were supposed to be linked to three different vortex structures, which form at the nozzle lip and quickly develop in the near field. Two of them originated as structures of azimuthal vorticity and the third one is a structure of axial vortices. The strongest azimuthal structure and the axial structure are supposed to be related to the well-known axial and azimuthal instabilities of jets, through the Kelvin–Helmholtz and Corcos and Lin [2] mechanisms. The third structure appears to be deeply linked to the high forcing. It seems to be, initially, an azimuthal vorticity structure, appearing interleaved in the array of Kelvin–Helmholtz vortex rings and with opposite sign of vorticity. These vortices are supposed to be caused mainly by the induction of the Kelvin–Helmholtz vortices as they move away from the nozzle exit. Other mechanisms related to the concentration of such vortical structure are commented in [1], along with a discussion of the possible interactions between structures and the resulting configurations that the mixing layer adopts.

This previous work defined the different configurations and presented a general model of the inviscid vortex dynamics, but being based on visualisations, lacked of a quantitative validation. Moreover, the flow was laminar, with a Reynolds number of 440 (based on the nozzle diameter and the mean velocity difference between co-flowing streams). The lack of quantitative

* Corresponding author.
E-mail address: ulpiano@ing.uc3m.es (U. Ruiz-Rivas).

0997-7546/02/$ – see front matter
PII: S0997-7546(02)01210-4

measurements is fulfilled in the present work with simultaneous whole-field velocity measurements obtained with the 2D-PIV technique (Adrian [3], Willert and Gharib [4]). Also, the flow studied here involves Reynolds numbers in the range 4000–8000, extending from laminar to transitional flows, which have a broader scope and a wider range of possible industrial applications.

The flow under study is of high industrial interest. The axial forcing produces an organised growth of definite modes of the jet instability. This brings the possibility of enhancing the jet entrainment, so that less power is needed for devices that nowadays rely on this kind of flows for mixing and heat or mass transferring. Besides, choosing the growth of favourable modes instead of leaving the natural jet structure to develop could reduce the noise emitted by a high-speed jet. The work in these fields has been reviewed by Gutmark and Grinstein [5].

2. Experimental facility

The experiments were conducted in a horizontal water tunnel. Fig. 1 shows a longitudinal section of the tunnel. Only a short description of the facility will be given here. Ruiz-Rivas [6] offers a more detailed description.

The water tunnel consists of two independently created, low speed streams. The inner stream is produced through a round nozzle of inner diameter $D = 15$ mm, located downstream of a settling chamber. A slower, co-flowing stream of square cross-section surrounds the inner jet. The two streams meet in a box of 200×200 mm square cross-section, which has lateral walls of transparent metacrilate to allow PIV measurements. The flow is evacuated through two lateral apertures at the end of the box. The distance between the nozzle exit and the end wall is $L = 41D$ (D is the nozzle diameter). At the design stage, it was checked that the perturbation introduced by the end wall would have a negligible effect on the flow at the test section. The argument is that, as the momentum of the natural jet diminish with the axial dimension as $(z/D)^{-2}$, the momentum of the jet at the end wall is very small, and its effect can be considered negligible. This was checked by means of numerical simulations, using the FLUENT®/UNS program and a standard k–ε model. It showed that the effect of the end wall on the axis flow velocity and the pressure distribution was negligible for $z/D > 10$ upstream from the end wall for the working conditions of our experiments. Fig. 2 shows the results of the FLUENT® simulation for the velocity in the axis with and without end wall. The end wall is also constructed of transparent metacrilate, providing a zenithal viewpoint of the flow.

The results reported here correspond to inner flow mean velocities, $u_{i,\mathrm{mean}}$, varying from 0.4 to 0.7 m/s and an outer flow mean velocity $u_0 = 0.1$ m/s. The inner velocity was chosen to have a "turbulent" Reynolds number ($Re_D > 5000$) and the outer velocity was chosen as high as possible, providing that the pressure in the tunnel will not affect our capability of forcing the inner jet.

The axial forcing is introduced through a vibrating membrane, located at the upstream end of the settling chamber of the inner flow and driven by a loudspeaker fed with a sinusoidal wave. The membrane motion adds an axial velocity monochromatic fluctuation of a given amplitude and frequency to the inner jet flow. Fig. 3 shows the axial velocity profiles along a forcing cycle for four different forcing amplitudes. The measurements were obtained with phase-locked PIV. Fig. 4 shows the velocity distribution on the flow axis along a forcing cycle and for the two extreme forcing amplitudes. The axial forcing frequency was set to 10 Hz during the experiments here reported. We have chosen a low forcing frequency because it gives a large wavelength of the vortex structures and therefore, more distinct structures.

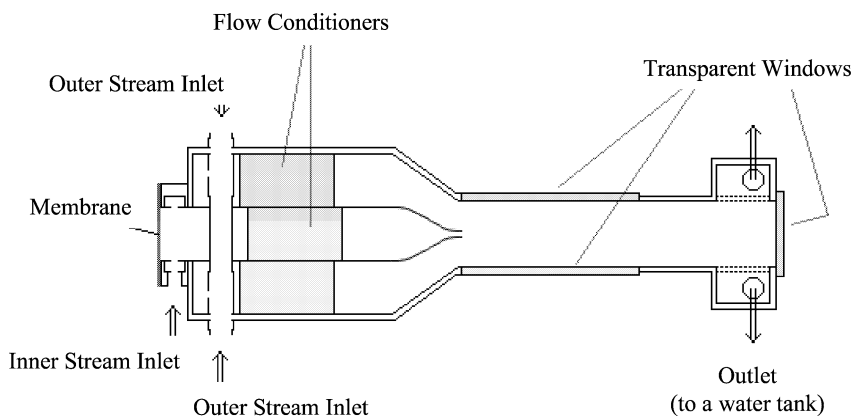

Fig. 1. Scheme of the flow facility.

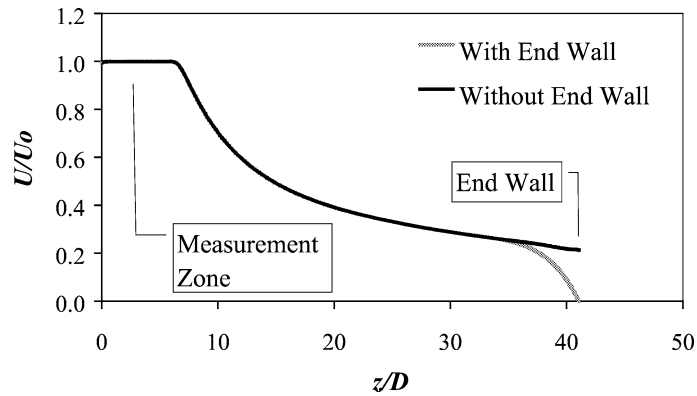

Fig. 2. Effect of the end wall in the measurement zone. The graph represents the axial velocity at the axis vs. the axial position from the nozzle exit, taken from numerical simulations, with and without end wall.

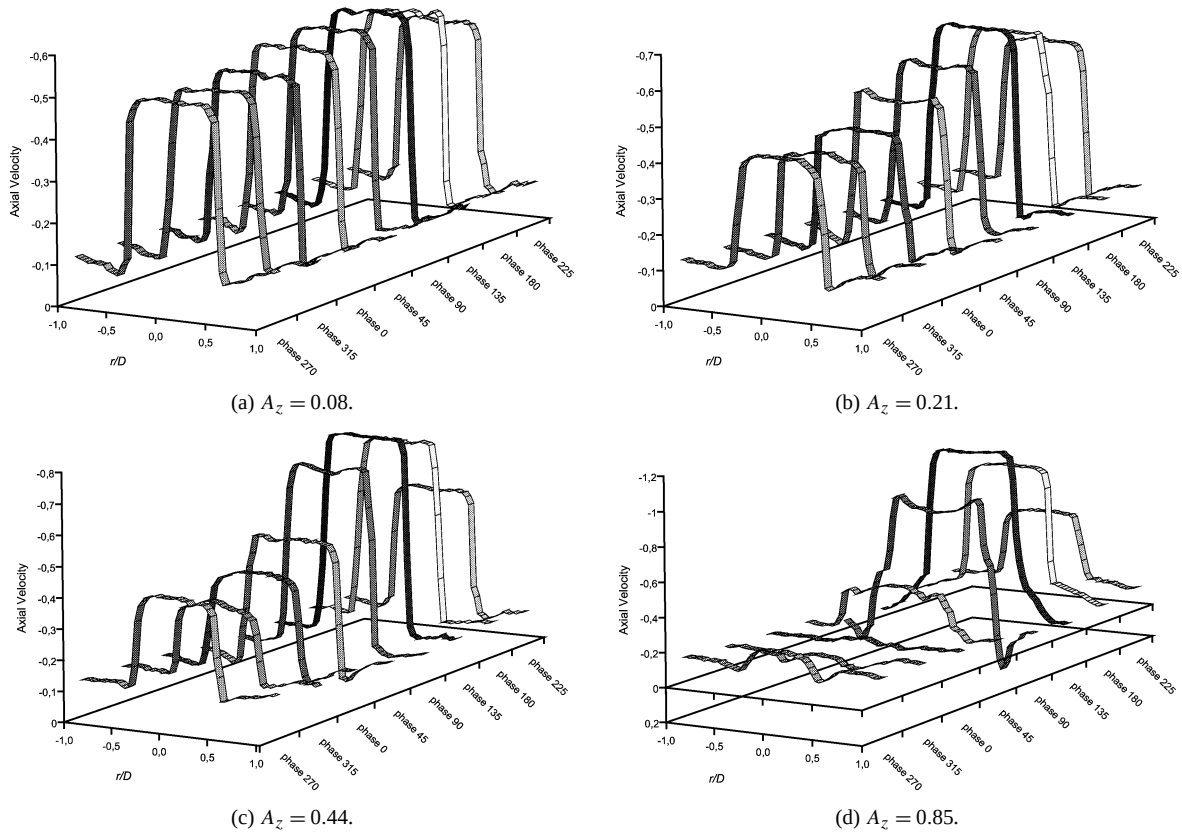

(a) $A_z = 0.08$. (b) $A_z = 0.21$.

(c) $A_z = 0.44$. (d) $A_z = 0.85$.

Fig. 3. Axial velocity profiles, obtained with PIV, for eight phases, equi-spaced along a forcing cycle, and for four different forcing amplitudes. The other non-dimensional parameters are: $Re = 8000$, $u_R = 0.2$, $St = 0.33$.

An azimuthal perturbation was introduced by using a 5-lobes indented nozzle exit, as in [1]. An indented nozzle is obtained machining the exit nozzle lip to a sinusoidal profile in the azimuthal and axial coordinates, $z_{\mathrm{Lip}} = A \cdot \sin(5 \cdot \theta)$. The sinusoidal profile had an amplitude $A = 1.5$ mm.

The relevant dimensionless parameters of the flow, as defined in [1], are the Reynolds number, *Re*, the Strouhal number, *St* (defined over the axial forcing frequency, f), the amplitude of the axial forcing, A_z, and the velocity ratio between inner and outer flow, u_R. The dimensionless parameters varied in the following ranges during the experiments:

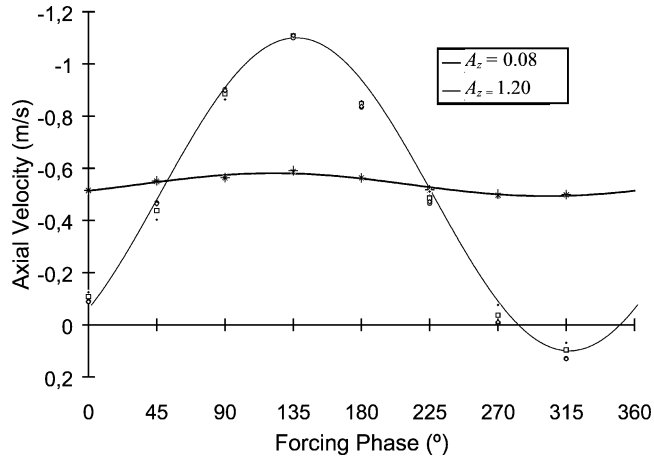

Fig. 4. Axial velocity on the axis along a forcing cycle, for the two extreme forcing amplitudes used during the experiments.

$$4000 < Re = \frac{(u_{i,\text{mean}} - u_0)D}{v} < 8000, \qquad 0.4 < St = \frac{fD}{(u_{i,\text{mean}} + u_0)/2} < 0.6, \qquad 0 < A_z = \frac{u_{i,\max} - u_{i,\min}}{u_{i,\max} + u_{i,\min}} < 1,$$

$$0.6 < u_R = \frac{u_{i,\text{mean}} - u_0}{u_{i,\text{mean}} + u_0} < 0.7.$$

3. PIV and flow visualisation techniques

The measurements of the velocity field have been obtained using the PIV technique. The DANTEC FlowMap® system has been used for the acquisition and processing of the images. Post-processing performed derivative calculation to obtain the vorticity and strain fields. The results presented here used a circulation filter (being one of the most widely used) for the derivatives. Our circulation filter has the following difference scheme:

$$\frac{\partial v_y}{\partial x} = \frac{1}{12}\frac{(v_{y(i+1,j+1)} + 4v_{y(i+1,j)} + v_{y(i+1,j-1)}) - (v_{y(i-1,j+1)} + 4v_{y(i-1,j)} + v_{y(i-1,j-1)})}{\Delta x}. \tag{1}$$

This is a little different from the typical scheme (Raffel et al. [7]). Both are low pass filters of the same order, but in this scheme, a parabolic fit is used for the points at $i-1$ and $i+1$, instead of the more typical linear fit. This gives a slightly better amplitude response at high spatial frequencies.

A scheme of the experimental facility can be seen in Fig. 5. The whole system is controlled from two PCs. PC1 controls the PIV system, stores the acquired images and vector maps and does all the post-processing. The PIV system is controlled through a processor that maintains the synchronisation between the camera and the illuminating system, which is constituted by

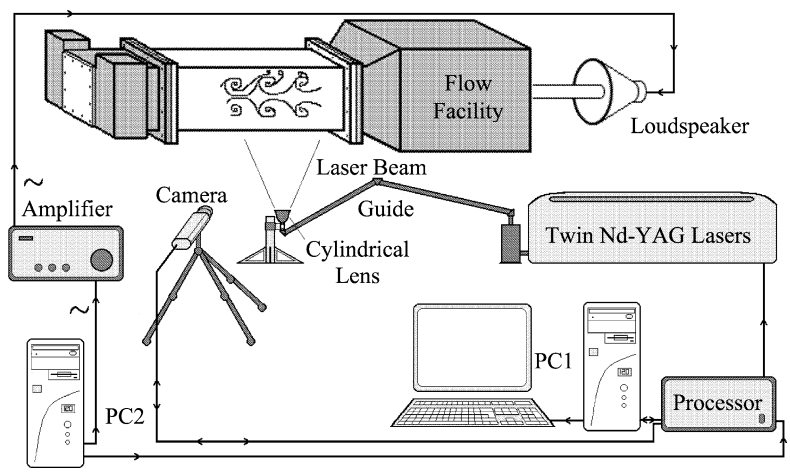

Fig. 5. Scheme of the experimental system.

two aligned 200 mJ Nd-YAG lasers, a beam guide and a cylindrical lens. The camera-guide-lens system was eventually rotated 90 degrees to obtain zenithal images for flow visualisation. On the other hand, PC2 generates the forcing signal, which feeds the loudspeaker through a power amplifier, controlling both frequency and amplitude of the forcing. PC2 also triggers the PIV system through the processor to get phase-locked measurements.

As the flow is different from that described in [1], due to the increased Reynolds number, several visualisation experiments were carried out using this same experimental system. The visualisations show the inner jet fluid, which is marked with a fluorescent dye (Rhodamine 6G). For the PIV measurements, both the inner and outer flow were seeded with sterilised commercial lycopodium spores, which are barely mono-dispersed ($d_l \sim 20$ μm) and almost neutrally buoyant, owing to their porous structure. The volume fraction between particles and fluid was in the 10^{-5}–10^{-4} range during our experiments. This can be assumed small enough to neglect the influence of the particles in the carrier flow (see, for example, Druzhinin and Elgobashi [8]).

The Stokes number of the lycopodium spores in the studied flow was around 10^{-3}, defined for the axial forcing frequency, so the drag force acting over the spores can be considered negligible. As for the other forces acting over a particle (added mass, unsteady pressure gradient—acceleration—and the Basset history), Hjelmfelt and Mockros [9] showed that, when the particle density approaches the fluid density, their effect is negligible in the whole frequency domain. Therefore, the seeding particles are expected to accurately trace the flow.

The field of view for the PIV measurements was varied along the experiments to match the opposed requirements of obtaining measurements in a wide area and with a high resolution. It ranged from areas of around 40×30 mm to 70×50 mm, taken by a 768×484 pixels CCD sensor camera. The thickness of the illuminating light sheet was around 1 mm, the mean image density (number of particles per interrogation window) was ~ 23, the image magnification was 18.6 pixels/mm or 0.22 mm/mm; the focal length of the imaging lens was 50 mm and its numerical aperture was 8. The cross correlation algorithm was carried out over areas of 32×32 pixels and with 75% overlapping, using sub-pixel peak fitting but no image deformation. The use of such a high overlapping (50% is more commonly used) may cause that, when there is correlated error in the data, the results in vorticity will show this correlated error more dramatically. Nevertheless, we have opted for the higher overlapping in order to give clearer images and the highest data yield. The possible incidence of correlated error will be discussed for each case.

The incidence of clear erroneous vectors was negligible, often zero, using standard algorithms for erroneous vector detection (moving average and range validation). The time between illuminating pulses was varied between 500 and 800 μs, in order to have maximum particle separations of around 1/4 of the interrogation window. The vector spacing obtained (8 pixels) was always below 1 mm (in both r and z). The spatial resolution is defined by a 32×32 pixels cell, the interrogation window size, as stated by Willert and Gharib [4] and is 1.7×1.7 mm. A cell denoting the size of the interrogation window will be printed in the velocity and vorticity field graphs of Section 5. The velocity resolution varied between 1 and 3 mm/s. Higher resolutions could be easily obtained, but the high velocity gradients that appear in the near field of the co-flowing jets would produce erroneous measurements on the shear layer, as predicted by Huang et al. [10]. Peak locking (Westerweel [11]) may be slightly present in the results, as the mean particle diameters were around 1.1 pixels. The mean displacement was around 4 pixels and it can reach up to 8–10 pixels, thus minimising the relative importance of this effect.

Due to the limitations of the measurement technique, some of the vortical structures that will be shown in the results of Section 5 may be partially affected by noise or artefacts from the measuring technique. This will be discussed in detail later. Nevertheless, it should be noted that the results shown in this article are withdrawn from some hundreds of results obtained for the same conditions and phases. The structures that will be discussed later appear in a vast majority of these measurements, thus diminishing the possibility that an erroneous measurement will have lead us to a mistaken inference. The quantitative measurements are backed by extensive studies of flow visualisation. Therefore, the incidence of noise or the appearance of artefacts of the measurement technique may slightly affect the value of the vorticity peaks, its width and its shape, but cannot be erroneously identified as a vortical structure of the flow.

Moreover, some of the results obtained during the experiments presented here were studied using different PIV and derivative algorithms, in order to establish the possible incidence of errors in the vorticity calculation. The results are presented in Ruiz-Rivas et al. [12], showing similar physical characteristics, independent on the PIV algorithm (the here described conventional algorithm in front of the high resolution LFC PIV algorithm of Nogueira et al. [13]) and the derivative filter used for vorticity calculation.

4. Velocity field post-processing

Several other variables can be derived from the u_z, u_r velocity fields obtained by PIV. The azimuthal component of the vorticity can be obtained by:

$$\vec{\omega}_\theta = \left(\frac{\partial v_r}{\partial z} - \frac{\partial v_z}{\partial r} \right) \vec{u}_\theta . \tag{2}$$

Also, the rate of strain can be quantified from the velocity field, but several considerations must be taken into account. The strain tensor (Panton [14]) can be written as:

$$\sigma_{ij} = \begin{bmatrix} \frac{\partial v_r}{\partial r} & \frac{1}{2}\left(r\frac{\partial}{\partial r}\left(\frac{v_\theta}{r}\right) + \frac{1}{r}\frac{\partial v_r}{\partial \theta}\right) & \frac{1}{2}\left(\frac{\partial v_r}{\partial z} + \frac{\partial v_z}{\partial r}\right) \\ \frac{1}{2}\left(r\frac{\partial}{\partial r}\left(\frac{v_\theta}{r}\right) + \frac{1}{r}\frac{\partial v_r}{\partial \theta}\right) & \frac{1}{r}\frac{\partial v_\theta}{\partial \theta} + \frac{v_r}{r} & \frac{1}{2}\left(\frac{1}{r}\frac{\partial v_z}{\partial \theta} + \frac{\partial v_\theta}{\partial z}\right) \\ \frac{1}{2}\left(\frac{\partial v_r}{\partial z} + \frac{\partial v_z}{\partial r}\right) & \frac{1}{2}\left(\frac{1}{r}\frac{\partial v_z}{\partial \theta} + \frac{\partial v_\theta}{\partial z}\right) & \frac{\partial v_z}{\partial z} \end{bmatrix}. \tag{3}$$

We should consider the velocity field in terms of the average and non-average quantities. The instantaneous velocity obtained can be de-composed as:

$$v_i = \bar{v}_i + \langle v_i \rangle + v_i' \quad \text{for } i = r, z, \theta. \tag{4}$$

Where $\bar{v}_i$ denotes the mean velocity in a certain position, $\langle v_i \rangle$ is the average for a certain phase of the forcing signal and v_i' is the non-averaged term. Due to the lobed shape of the nozzle, all diametrical planes are not symmetry planes, but the measurement plane is a symmetry plane of the lobed nozzle. Therefore, the averaged quantities of the velocity will be symmetrical and, in the measurement plane:

$$\bar{v}_\theta + \langle v_\theta \rangle = 0, \quad \frac{\partial t(\bar{v}_r + \langle v_r \rangle)}{\partial \theta} = 0, \quad \frac{\partial(\bar{v}_z + \langle v_z \rangle)}{\partial \theta} = 0. \tag{5}$$

With such conditions, the strain tensor can be simplified, yielding:

$$\sigma_{ij} = \begin{bmatrix} \frac{\partial v_r}{\partial r} & \frac{1}{2}\left(r\frac{\partial}{\partial r}\left(\frac{v_\theta'}{r}\right) + \frac{1}{r}\frac{\partial v_r'}{\partial \theta}\right) & \frac{1}{2}\left(\frac{\partial v_r}{\partial z} + \frac{\partial v_z}{\partial r}\right) \\ \frac{1}{2}\left(r\frac{\partial}{\partial r}\left(\frac{v_\theta'}{r}\right) + \frac{1}{r}\frac{\partial v_r'}{\partial \theta}\right) & \frac{1}{r}\frac{\partial v_\theta}{\partial \theta} + \frac{v_r}{r} & \frac{1}{2}\left(\frac{1}{r}\frac{\partial v_z'}{\partial \theta} + \frac{\partial v_\theta'}{\partial z}\right) \\ \frac{1}{2}\left(\frac{\partial v_r}{\partial z} + \frac{\partial v_z}{\partial r}\right) & \frac{1}{2}\left(\frac{1}{r}\frac{\partial v_z'}{\partial \theta} + \frac{\partial v_\theta'}{\partial z}\right) & \frac{\partial v_z}{\partial z} \end{bmatrix}. \tag{6}$$

The first invariant of the rate of strain field is the sum of the squares of the different rates of strain. The square root of the first invariant may be an appropriate measurement of the rate of strain (Bradshaw and Koh [15]). The $(2, 2)$ term of the tensor in Eq. (6) can be obtained from the u_z, u_r velocity fields using the continuity equation for incompressible flow:

$$\frac{v_r}{r} + \frac{\partial v_r}{\partial r} + \frac{1}{r}\frac{\partial v_\theta}{\partial \theta} + \frac{\partial v_z}{\partial z} = 0. \tag{7}$$

The resulting expression for the square root of the first invariant of the strain tensor is:

$$\sigma = (2\sigma_{ij}\sigma_{ij})^{1/2} = \left[2\left(\frac{\partial v_r}{\partial r}\right)^2 + 2\left(\frac{\partial v_z}{\partial z}\right)^2 + \left(\frac{\partial v_r}{\partial z} + \frac{\partial v_z}{\partial r}\right)^2 + 2\left(\frac{\partial v_r}{\partial r} + \frac{\partial v_z}{\partial z}\right)^2 + \left(r\frac{\partial}{\partial r}\left(\frac{v_\theta'}{r}\right) + \frac{1}{r}\frac{\partial v_r'}{\partial \theta}\right)^2 + \left(\frac{1}{r}\frac{\partial v_z'}{\partial \theta} + \frac{\partial v_\theta'}{\partial z}\right)^2\right]^{1/2}. \tag{8}$$

The factor 2 inside the square root is used to provide a good comparison with vorticity, as shown by Bradshaw and Koh [15] and others.

Note that the two last terms on the right side of Eq. (8) involve only non-averaged quantities. These terms can be considered small compared with the rest of the terms of the equation. Therefore, a good approximation for the square root of the contraction of the strain tensor can include only the u_z, u_r velocity fields, that is, the measured components:

$$\sigma \approx \left[2\left(\frac{\partial v_r}{\partial r}\right)^2 + 2\left(\frac{\partial v_z}{\partial z}\right)^2 + \left(\frac{\partial v_r}{\partial z} + \frac{\partial v_z}{\partial r}\right)^2 + 2\left(\frac{\partial v_r}{\partial r} + \frac{\partial v_z}{\partial z}\right)^2\right]^{1/2}. \tag{9}$$

The information of the strain field may be better understood if compared with the local azimuthal vorticity. Hence, a local parameter, χ, has been defined as:

$$\chi = \frac{\sigma^2 - \omega^2}{\sigma^2 + \omega^2}. \tag{10}$$

This coefficient separates three different zones in the flow field, as exposed by Tanaka and Kida [16]: line vortices or zones where the vorticity is dominant ($\chi < 0$); deformation cells or zones where the strain is dominant ($\chi > 0$); and vortex sheets or zones were both magnitudes are large ($\chi \sim 0$). The zones where both the azimuthal vorticity and the strain are small will be withdrawn, as the information of the coefficient there will mainly contain background noise.

Another interesting parameter is the pressure distribution. Bradshaw and Koh [15] found that, for an incompressible flow, the application of the gradient operator to the momentum equation leads to:

$$-\frac{\nabla^2 p}{\rho} = \frac{\sigma^2 - \omega^2}{2}. \tag{11}$$

Finally, some information can be drawn for the third velocity component. For estimation, we will try to get some information of the averaged fields. Eq. (5) shows that the averaged azimuthal velocity component must be zero in the measuring plane, due to the flow symmetry, but its azimuthal derivative is nonzero and can be obtained from the continuity equation (7). In can also be shown that the second azimuthal derivative of the averaged azimuthal velocity is zero, deriving the continuity equation for the azimuthal coordinate and keeping in mind the simplifications of Eq. (5). Therefore, the information available about the azimuthal velocity is:

$$\bar{v}_\theta + \langle v_\theta \rangle = 0, \qquad \frac{1}{r}\frac{\partial(\bar{v}_\theta + \langle v_\theta \rangle)}{\partial\theta} \approx \frac{v_r}{r} - \left(\frac{\partial v_r}{\partial r} + \frac{\partial v_z}{\partial z}\right), \qquad \frac{\partial^2(\bar{v}_\theta + \langle v_\theta \rangle)}{\partial\theta^2} = 0. \tag{12}$$

5. Results

This study is strongly supported by the qualitative results presented in Rodríguez et al. [1]. Nevertheless, the measurements presented here were carried out in a different flow facility and at different Reynolds number. Therefore, a visualisation study of the flow was first performed. It allows verifying the inviscid nature of the main mechanisms that control the development of the vortical structures in the near field. Next, PIV measurements were performed and the resulting velocity maps allowed drawing some conclusions about the flow development. Finally, the derived quantities, such as vorticity and strain, were obtained and the near field vortex dynamics could be quantitatively explored.

This procedure was followed for several configurations defined by different forcing amplitudes. Two configurations, a low forcing configuration and a high forcing configuration will be explained here in detail. The change in forcing amplitude leads to two very different near field flow configurations, which are typical of the studied amplitude range. Only the high forcing case was addressed in [1].

5.1. Visualisation of the flow

Figs. 6 and 7 show visualisations of the co-flowing jets for $Re = 4500$ and a low forcing frequency. The inner jet is visualised in black due to the injection of a fluorescent dye in the inner stream.

Fig. 6 shows flow visualisations for a low forcing amplitude configuration, while Fig. 7 shows the high forcing amplitude case. The jet lateral spread in the low forcing case (Fig. 6) concentrates in azimuthal positions aligned with the crests of the indented nozzle and it is rather small. The lateral spread in the high forcing case (Fig. 7) appears to concentrate at azimuthal positions aligned with the valleys of the indented nozzle, although they are not as clear as those in the preceding case. Also, their lateral amplitude is larger. The full aperture of the jet in such locations reaches a very large angle, of approximately 70°. The initial organisation of the zones of lateral spread can be better visualised in the crosscuts of Fig. 8, taken at $z = D/2$ (nearer to the nozzle) on a flow of slightly higher Reynolds number.

The images of Figs. 7 and 8 are similar to those studied in [1] for the low Reynolds number case, but the images of Fig. 6 show a different mode. In this case, the jet lateral spread is smaller and shifted in its azimuthal location, but it is larger than in the unforced case. This is easily visualised in the longitudinal cuts, which show the lateral development of inner fluid in crest-aligned locations, a development that persists and even enhances when the flow develops a transition. The crosscuts show the existence of pairs of streamwise (axial) eddies in the zone, and also show that those eddies have some continuity from one braid [1] to the next.

The high forcing amplitude case of Fig. 7 represents similar configurations to the ones observed in the laminar flows studied in [1]. The forcing conditions for which this flow organisation appears are also in good agreement with those observed in [1]. Hence, the minor importance of the Reynolds number is corroborated and the hypothesis of inviscid mechanisms taken place is validated.

Based on the visualisations, a qualitative explanation of the near-field vortex dynamics has been elaborated for each case. Figs. 9 and 10 respectively show the vortex structure arrangement for the high and the low amplitude cases, each filament representing a vortex. Fig. 9 is a re-elaboration of those shown in [1] and is fully compatible with the reasoning and the visualisations given there, so we will not repeat them here. All the implications of the qualitative model presented in [1] are in accordance with the results presented in Figs. 7 and 8, so we will not explain them further. On the other hand, the processes that are observed in the low forcing configuration were not studied in [1]. Therefore, a kinematic explanation follows. The

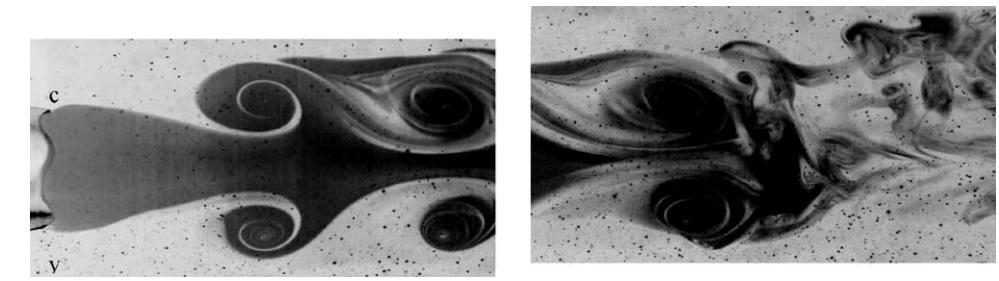

(a)

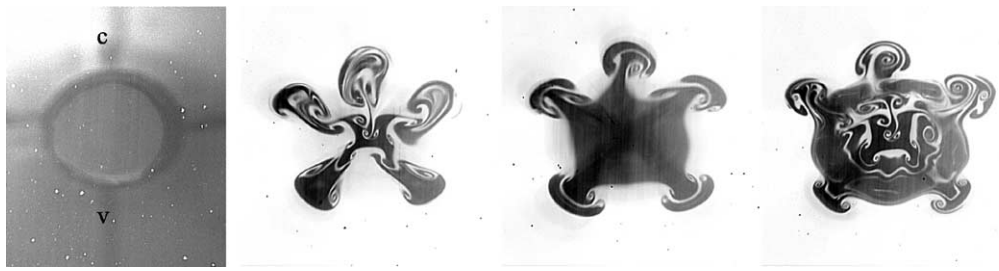

(b)

Fig. 6. Longitudinal cuts and crosscuts for the low forcing amplitude case. The flow conditions are $Re = 4500$, $u_R = 0.6$, $St = 0.6$ and $A_z = 0.3$. (a) Longitudinal cuts along the flow axis. Flow comes from left to right. The two images show the flow field from $z = 0$ to $4D$ and from $4D$ to $8D$ for the same phase but they are not taken in the same instant. (b) Crosscuts at $z = 2D$ for three equi-spaced phases along a forcing cycle. A crest (c) of the indented nozzle is on top and a valley (v) on bottom of the images.

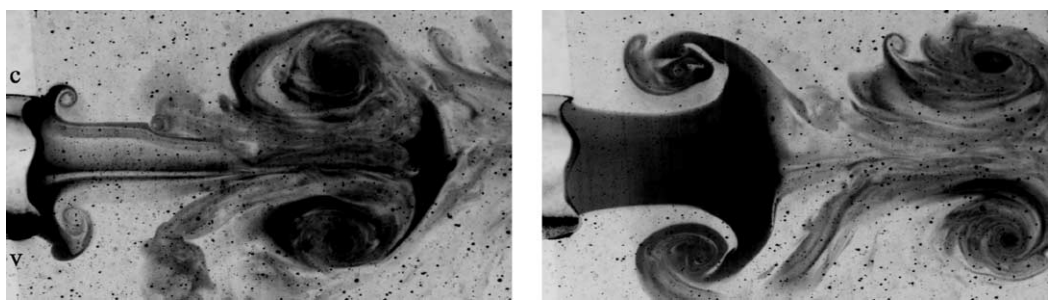

(a)

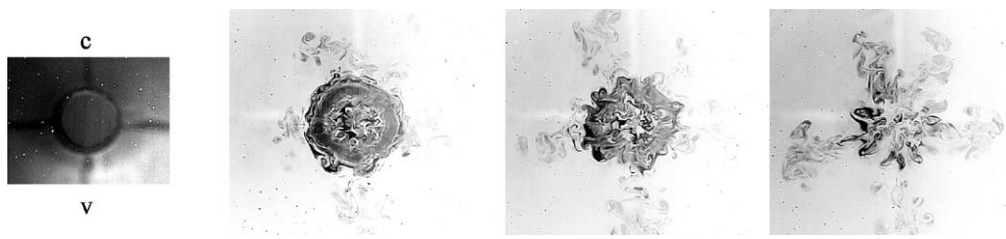

(b)

Fig. 7. Longitudinal cuts and crosscuts for the high forcing amplitude case. The flow conditions are $Re = 4500$, $u_R = 0.6$, $St = 0.6$ and $A_z = 0.9$. (a) Longitudinal cuts along the flow axis. Flow comes from left to right. The two images show the flow field from $z = 0$ to $4D$ for two phases separated by a half-period. (b) Crosscuts at $z = 2D$. The left image shows the nozzle exit for reference. A crest (c) of the indented nozzle is on top and a valley (v) on bottom of the images.

processes shown in Fig. 6 can be explained in terms of the kinematics of two vortical structures formed in the vicinity of the nozzle lip. These structures are the well-known primary structure (an array of vortex rings periodically distributed along the axial coordinate) and the secondary structure studied by Liepmann and Gharib [17] (an array of streamwise vortices periodically

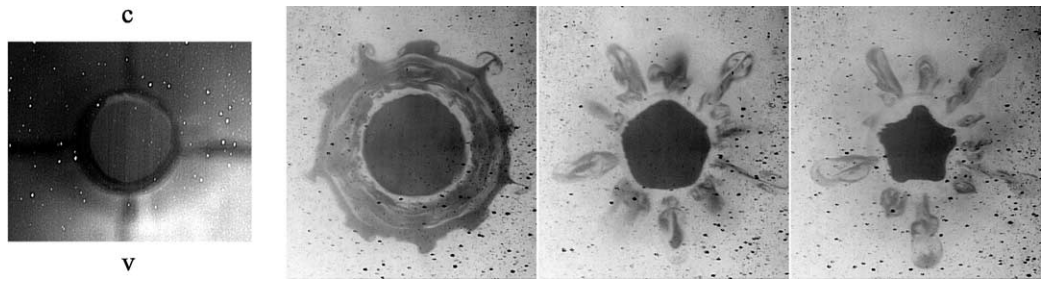

Fig. 8. Crosscuts at $z = D/2$ for the high forcing amplitude case. Three equi-spaced phases along a forcing cycle. The flow conditions are $Re = 7000$, $u_R = 0.7$, $St = 0.45$ and $A_z = 0.9$. The left image shows the nozzle exit for reference. A crest (c) of the indented nozzle is on top and a valley (v) on bottom of the images.

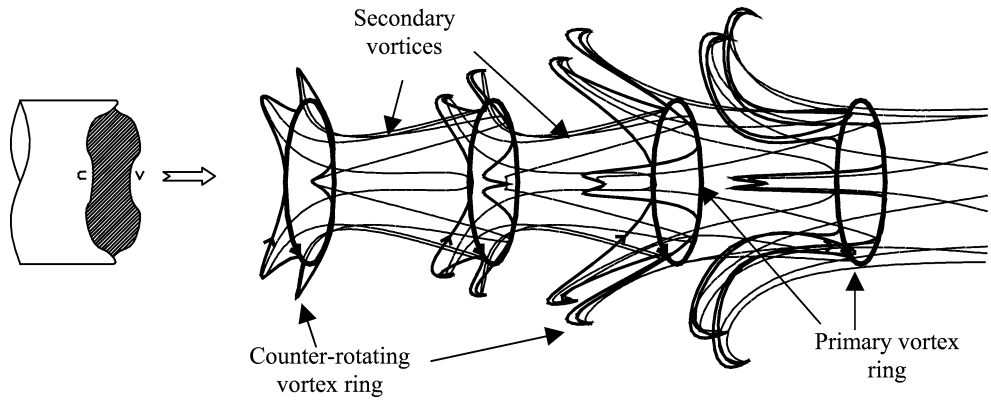

Fig. 9. Qualitative description of the near-field vortex dynamics for the high forcing amplitude case.

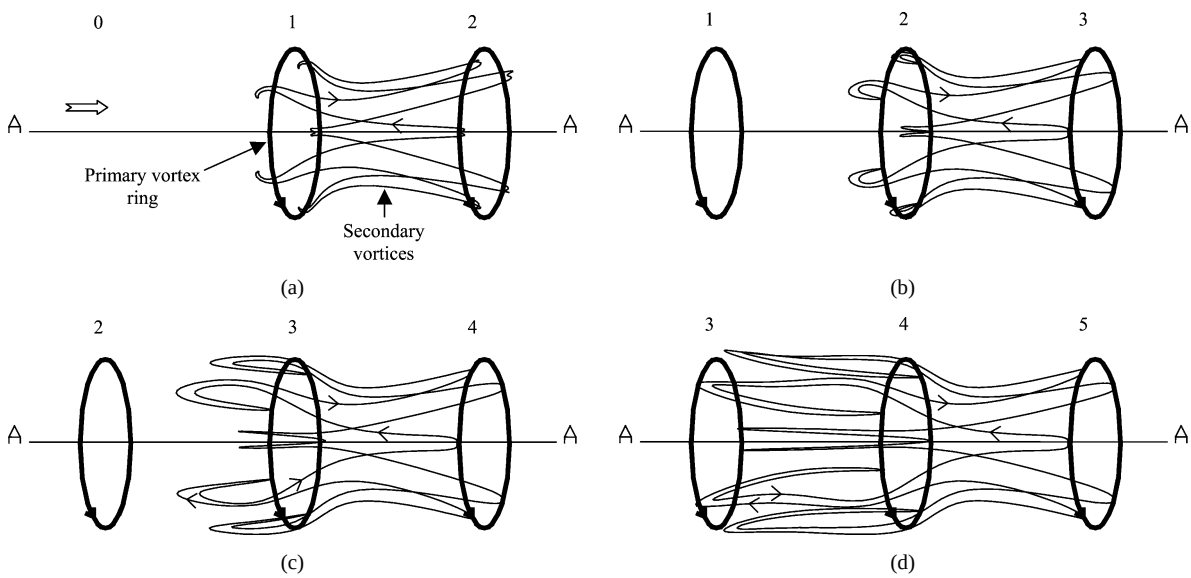

Fig. 10. Qualitative description of the near-field vortex dynamics for the low forcing amplitude case. A sequential presentation is chosen to avoid confusion between streamwise vortices coming from two consecutive braids. Therefore, only the structure that is originated in the second braid is plotted.

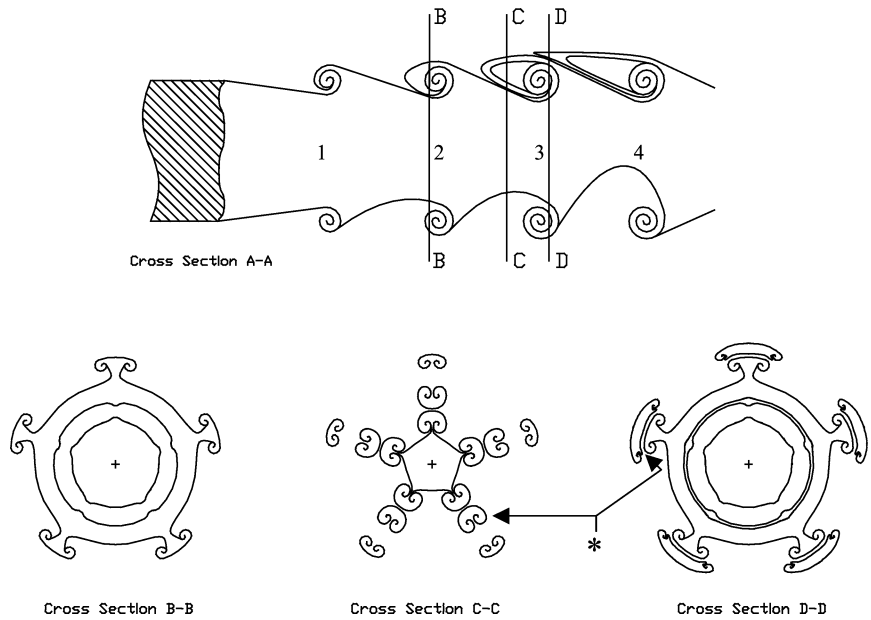

Fig. 11. Sketch of the evolution of the mixing layer due to the near-field vortex dynamics presented in Fig. 10. Cross-section AA is defined on Fig. 10 and cross-sections BB, CC and DD are defined over section AA.

distributed along the azimuth). Due to its nature and relative initial positioning, they develop several processes, which can be observed in the visualisations. An extensive presentation of the images obtained during the visualisations is presented in [6]. The motion of the structures is as follows:

(a) The secondary structure develops from the braids and into the vortex cores.
(b) As the secondary structure develops around the primary vortex core and to its upstream side, an axial deceleration seems to appear. Considering its previous motion, in this zone the structure should take the form of two parallel filaments. Therefore, the deceleration may be interpreted as a self-induced motion. The two parallel filaments should induce a velocity in each other. Such velocity may be of relevance, in despite of the low vorticity of the filaments, due to their proximity, considering the Biot–Savart mechanism. Thus, retardation is imposed to the structure in this zone, and it develops (relatively) upstream in the next braid.
(c) When the parts of the structure that are being retarded reach the centre of the braid, the process is accelerated. This can be explained by the effect of the induction of the oncoming vortex ring, which adds up to their self-induced motion.
(d) The secondary structure continues its motion over the oncoming vortex ring and into the next braid (which is now the second braid upstream to that in which the structure was actually formed). This process can be explained taken into account the two forces explained in (c).

These processes have been depicted in Fig. 10, in a similar way as it was done in Fig. 9. For a better understanding of Fig. 10, a sketch of the implications over the mixing layer has been drawn in Fig. 11.

The important feature here is that the complex 3D structure of the flow is well fitted, although the processes that were considered to draw Figs. 9 and 10 are rather simple. First, they are all inviscid processes, concerning with the kinematic motion of the vortices and their mutual interactions represented by a Biot–Savart scheme. Furthermore, only two or eventually three structures have to be considered, of which the origin has been explained. In the case of the two structures in the low forcing case, their evolution has been widely stated in the literature (for example, Liepmann and Gharib [17], Martin and Meiburg [18], Grinstein et al. [19], Brancher et al. [20], etc.). The mechanisms of formation and development are similar, although the dynamics observed here are rather different from the observed by those authors, due to the finite forcing used.

5.2. PIV velocity fields

Fig. 12 shows the velocity field at four different times (four equi-spaced phases in a forcing cycle) and for the two flow configurations observed in the visualisations. In the high amplitude case, the field of view is shifted to a close-up view of a

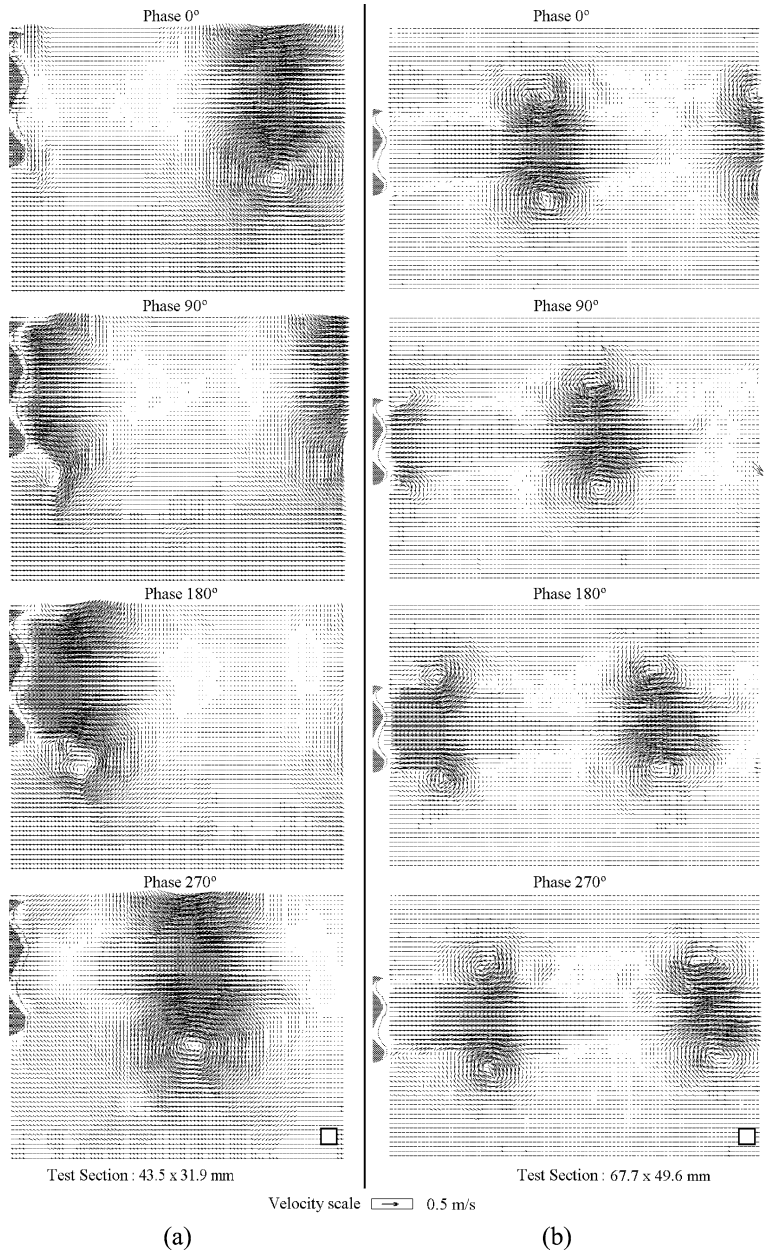

Fig. 12. PIV measurements of the axial and radial velocity components. The flow conditions are $Re = 7000$, $u_R = 0.7$ and $St = 0.45$. (a) High forcing amplitude case, $A_z = 0.9$. (b) Low forcing amplitude case, $A_z = 0.5$. A crest of the indented nozzle is on top and a valley on bottom of the graphs, as shown by the sketch of the nozzle on the left side of each graph. The square in the lower right side represents the interrogation window size.

valley-aligned position in order to get a higher resolution (in PIV measurements both the velocity and the space resolution are related to the pixel discretisation). The crest-aligned positions would show a similar base structure except for the most-interesting lateral development. In the low forcing case a larger field of view area was chosen.

The incidence of erroneous vectors was negligible, so no interpolation algorithms have been used with these data.

For a better understanding, the global mean velocity of the vectors in each graph has been subtracted. The global mean is a vector in the axial direction and is almost constant (being the field of view large enough) for the different phases of each case.

The graphs of Fig. 12 reveal the existence of strong primary ring vortices. These vortices quickly form and create a velocity field in their surroundings. This velocity field is super-imposed to the base field and it generates large radial velocities. Of

special relevance is the fact that the strong vortices of graphs (a), phases 180° and 270°, induce inbound radial velocities at the nozzle lip.

As shown in [1], the incidence of such velocities at the nozzle lip will be a new source of vorticity. If this vorticity concentrates, it will produce a vortex structure, which will be composed of counter-rotating vortex rings generated in the braids between two vortex rings of the primary structure. Also note that, as the velocities induced by the primary vortices produce these new vortices, their vorticity will be weak in comparison to that of the primary structure. A similar mechanism has been reported in the well-known work of Didden, which appears in the album of Van Dyke [21]. Therefore, this result support the hypothesis made in [1] for the origin of the third vortex structure.

The effect is smaller in the low forcing case. The primary vortices are weaker; thus the velocities induced at the nozzle lip are smaller. If the induced velocities are very small, the counter-rotating vorticity will not concentrate in a vortex, but will remain distributed. This seems to be the case for the low forcing configuration.

The presentation of the vector field in Fig. 12 can be misleading in that the observer may see negative axial velocities. Actually, in these graphs all the axial components are positive, but the subtraction of the global mean may lead to this error.

Low velocities (of the order of the global mean) appear in the inner region of the braids. Note that this effect is amplified for the high forcing case, once again due to stronger vortices and therefore larger induction. The stronger vortices of the high forcing case concentrate more rapidly, and the braid shear layer vanishes.

5.3. Derived fields

Figs. 13 and 14 show the vorticity fields for different phases of the forcing signal. The fields were obtained using Eq. (1) over the PIV data. Fig. 13 shows the high-amplitude, three-structure case and Fig. 14 shows the low-amplitude, two-structure case. Fig. 13 shows 8 phases to provide a closer follow-up of the counter-rotating vortex structure development in valley-aligned locations.

The presence of the nozzle lip introduces erroneous measurements of the velocity, as it scatters light. Therefore, large errors appear in vorticity in the very near surrounding of the nozzle. These values are, of course, non-physical, as the measurements are taken over a static solid, but they are kept to preserve objectivity. Sometimes it is difficult to decide whether the local value of the vorticity is due to the generation of a vortex in the zone (as happens near the lower lip) or due to this error. The effect is more evident near the nozzle axis, where vorticity disappear or changes sign from one recording to the following, which is of course unreal.

Some spurious, small amplitude vorticity is spread all over the vorticity field, owing to its derivative-based nature. Its elimination by a low-pass filter would smooth the vorticity peaks from the actual vortices, something that is undesirable. A critical analysis of the errors attributable to the PIV technique indicates that the error could be in the order of one to two iso-contours, shown in Figs. 13 and 14. Also, a small box on the lower right side shows the size of the interrogation window.

A striking feature of the primary vortical structures shown in Figs. 13 and 14 is that the vorticity distribution in a vortex is not symmetrical. Instead of that, they seem to be formed by several closely grouped peaks, rotating as a consequence of their mutual induction. This phenomenon was also observed in Ruiz-Rivas et al. [12], where we used completely different algorithms, both for the PIV measurement and for the derivative calculation. Raffel et al. [7] reported that the use of 75% overlapping instead of 50% gives higher vorticity peaks and less smooth contours. Their experiments were done over a laminar vortex, so a smooth contour was more physical, but the actual statement of the maximum vorticity is still a subject of discussion. On the other hand, the PIV data may show some peak locking [13], and it is difficult to state whether of not this effect may produce the observed organisation of vorticity.

The maps of Fig. 13 show two concentrations of azimuthal vorticity of opposite sign appearing at the nozzle exit lip around phase 0°. These are identified as the two vortex rings that were considered in the qualitative description of the flow presented in [1] and shown in Fig. 9. The downstream concentration, in light grey levels, represents the counter-rotating vortex ring and is here defined with negative values of the azimuthal vorticity, while the upstream concentration, in dark grey levels, represents the primary structure and is defined with positive values of the vorticity. Note that, due to the use of Cartesian coordinates (to avoid the axis definition over the PIV data), the sign of the vorticity in both structures is opposite above the axis. The other structure that was considered in [1], the secondary structure, consists of streamwise (axial) vorticity and cannot be observed in the r–z maps.

Let us first consider the development of a primary vortex ring. Following the vortex ring as phase increases, one can see its development: it first concentrates near the nozzle rim and then drifts downstream, remaining substantially axisymmetric. The position of these strong primary vortices is well defined in these graphs. Combining this information with the velocity fields and the mean velocities, we can calculate the convective velocity of the primary structure. In an unforced jet, the convective velocity of the structure is the mean velocity of the shear layer:

$$\bar{u}_{\text{s.l.}} = \frac{\bar{u}_{\text{inner}} + u_{\text{outer}}}{2}. \tag{13}$$

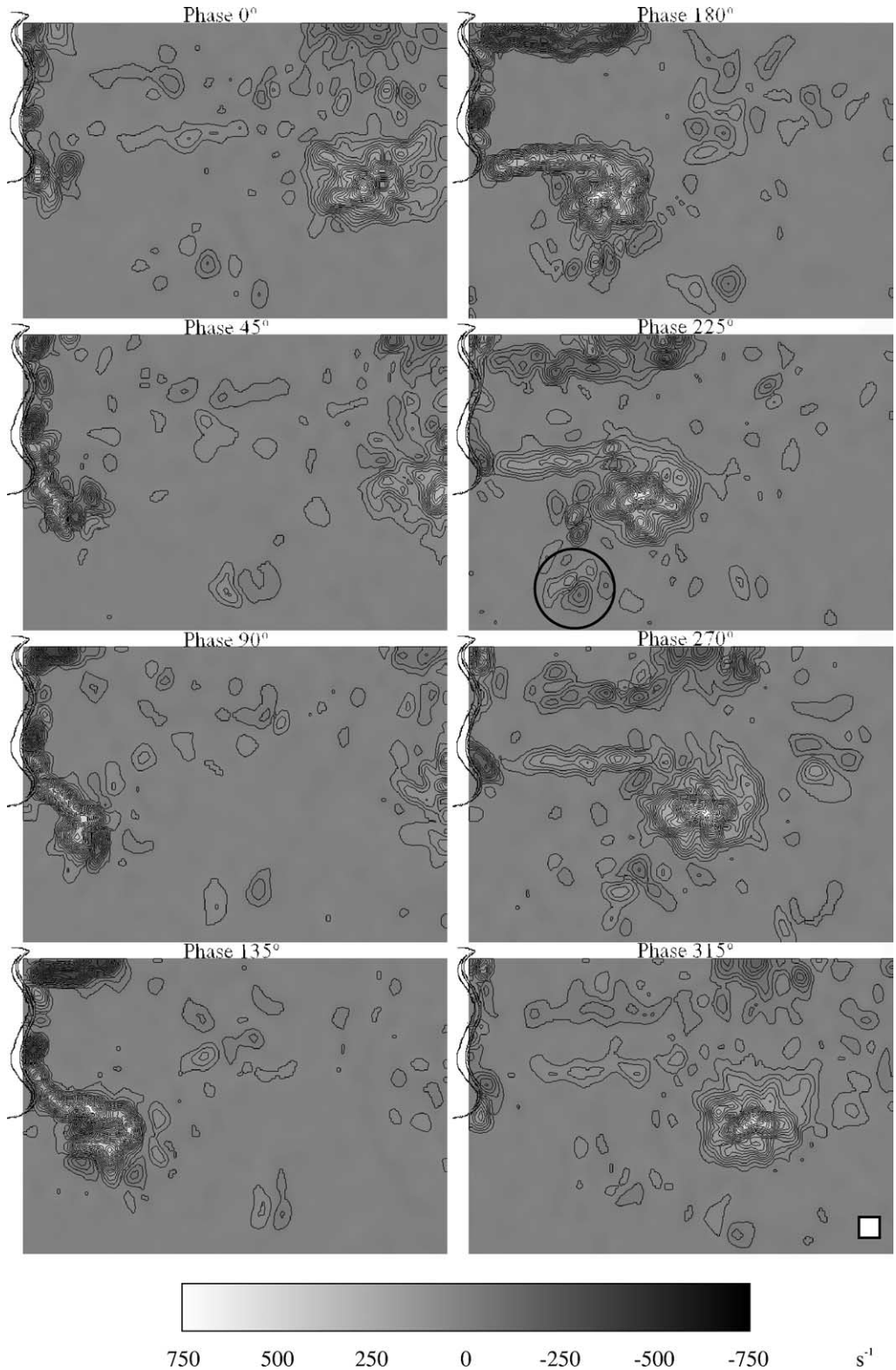

Fig. 13. Azimuthal vorticity maps for 8 equi-spaced phases along a forcing cycle. High forcing case, $A_z = 0.9$. The square in the lower right side represents the interrogation window size. Note that the medium grey tone represents zero vorticity.

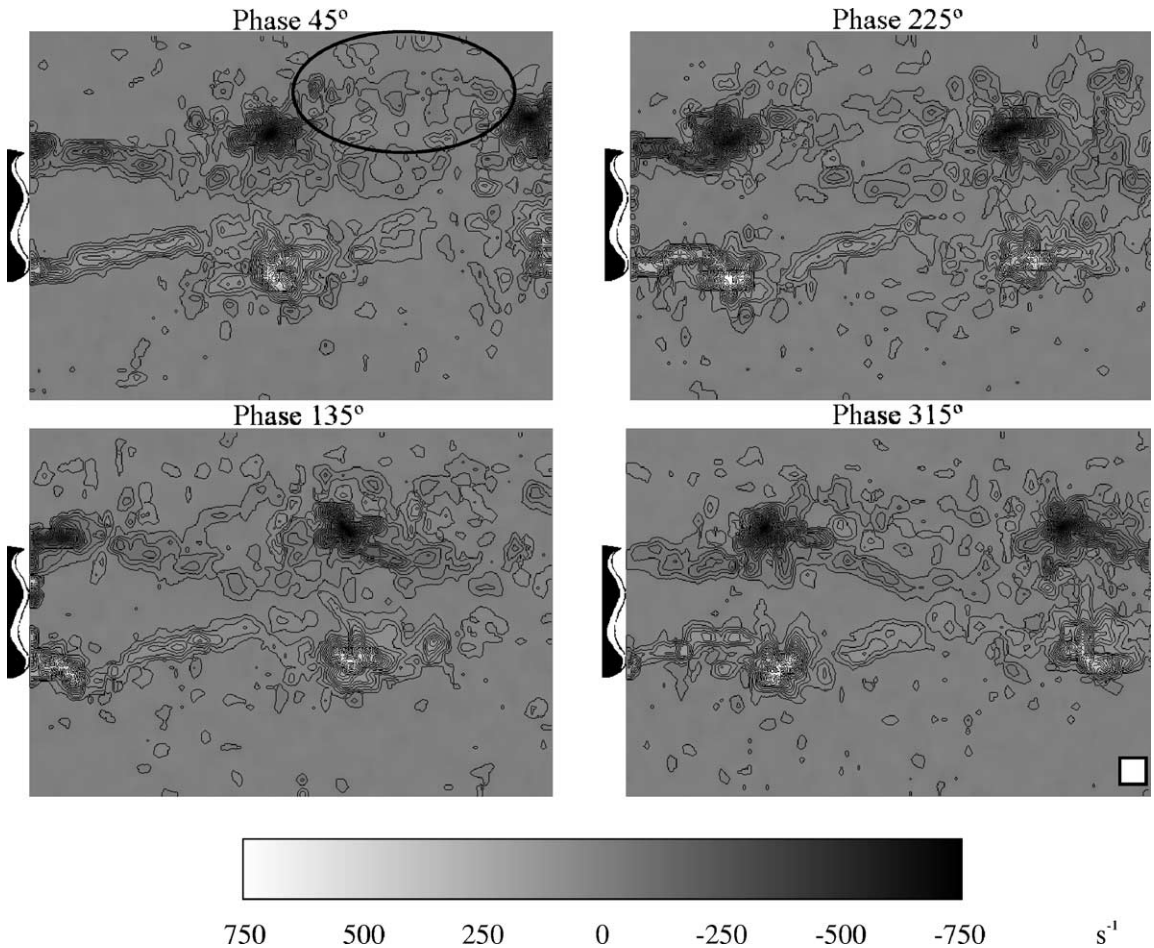

Fig. 14. Azimuthal vorticity maps for 4 equi-spaced phases along a forcing cycle. Low forcing case, $A_z = 0.4$. The square in the lower right side represents the interrogation window size. Note that the medium grey tone represents zero vorticity.

Nevertheless, the experiments show that, in an axially forced flow, the convective velocity of the vortex rings changes, depending on the forcing amplitude. Fig. 15 shows a comparison between the actual vortex velocity and the mean velocity of the shear layer, where large discrepancies can be observed.

The vortex convective velocity can be measured simply by dividing the spatial lapse between vortices that can be measured in the graphs of Figs. 13 and 14 by the laser pulse period. Nevertheless, it shall be considered that in the first instants of formation, the vortex is attached to the nozzle exit lip. In order to measure the free vortex convective velocity, the velocities were obtained only between vortices already detached from the lip. The instantaneous velocity fields of Fig. 12 provide a comparison and can be used to confirm that the velocity of the vortices is maintained constant after the detachment.

This constant velocity at which the vortices move seems to be better defined by a local convective velocity. It is defined over the maximum inner velocity, as the vortex location is triggered at the maximum value of the sinusoidal inner forcing:

$$u_{\text{conv}} = \frac{u_{\text{inner,max}} - u_{\text{outer}}}{2} = \frac{(A_z + 1)\bar{u}_{\text{inner}} - u_{\text{outer}}}{2}. \tag{14}$$

A comparison with the results is shown in Fig. 15 and yields an excellent agreement. This result is important for properly stating the primary structure wavelength and therefore the Strouhal number of the flow. It could be underestimated by almost a factor of 2 in the high forcing experiments if one considers the shear layer mean velocity as the vortex convective velocity, as has been done in earlier experiments. The wavelength of the primary structure controls the strain field intensity over the braids. Moreover, it defines the induction velocities that are involved in the origin of the counter rotating vortex rings and of the secondary structure, and in their development and amplification.

We will now focus in on the information given in Fig. 13 for the expected counter-rotating vortex structure. This structure follows a more complex development. Moreover, its smaller vorticity makes it more diffuse (in dark grey levels in Fig. 13).

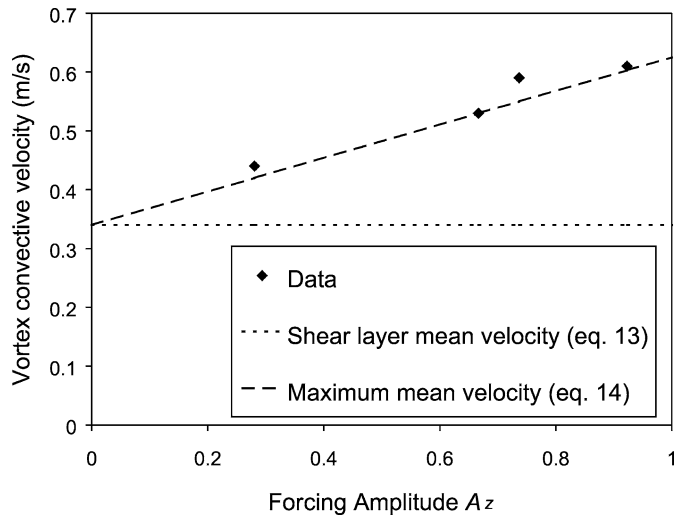

Fig. 15. Comparison of experimental data of the convective velocity of the primary vortex structure with predictions from Eqs. (13) and (14), for the range of forcing amplitudes investigated.

Anyway, it can be stated that, after its formation in the low-velocity half-period at the nozzle lip (phase 0° to 180°, it moves, developing a trajectory around the forming primary vortex ring. This motion seems to be due to the induction field of that primary vortex ring. Then, between phase 180° and 225°, the concentration of counter-rotating vorticity progressively separates from the primary vortex and begins to drift radially outwards and (relatively) upstream. At the same time, the counter-rotating vortex mutates into a pair of small-size vortices of opposite sign. This suggests, based in the dynamics sketched in Fig. 9, a reconnection mechanism between vortex filaments. Such mechanism would produce a closed vortex loop from the counter-rotating vortex ring. Such behaviour was predicted in [1], supported by the ideas of Martin and Meiburg [18] and Lasheras et al. [22]. This vortex loop would move radially outwards, self-propelled, and would show in these measurements as a pair of vortices of opposite signs (identified in Fig. 13 by a circle). As the flow develops, this structure moves laterally and gradually diminishes in vorticity.

It is interesting to note that the wavelength of the signal that gives the vortex pair identified by a circle in Fig. 13 is more than two times larger than the interrogation window size. This is also true in the other phase graphs. Therefore, its presence cannot be caused by a spurious vector or by correlated noise artefacts. Also, this structure repetitively appeared in repetitive measurements made during the experiments, a fact that, together with the visualisation study, gives a strong basis to consider it a vortex structure of the flow.

The measurements also show that, in his trajectory, this vorticity structure seems to leave behind a sequence of vorticity peaks of smaller amplitude. As it was stated above, it is not absolutely clear to the authors whether such peaks have a physical motive or appear due to a PIV technique numerical construction, thus being false. Nevertheless, the use of different algorithms in [12] with similar results seems to suggest that it does not have a spurious nature, although the measurements presented here cannot be considered conclusive. Their existence can be explained as follows: the region where these peaks of vorticity appear is a highly stretched one, and two quasi-axial vortex filaments are present in the near vicinity. Those filaments might break their initial azimuthal symmetry due to the high rate of strain, contributing to the field of azimuthal vorticity. On the other hand, the mere presence of such filaments may produce small perturbations in the velocity field that the PIV technique would present as vorticity due to minor velocity errors.

Fig. 14 shows the azimuthal vorticity fields for the low forcing case. Here the primary vortex ring is observed to appear near the nozzle lip, concentrate and drift more or less unperturbed. No organised concentration of counter-rotating vorticity is observed. Nevertheless, in the upper part (positions aligned with a crest) the vorticity field shows a distributed organisation (identified in Fig. 14 by an ellipse), that grows in vorticity when the two consecutive rings are formed. These concentrations of vorticity seem to be caused by the appearance in the zone of the structure observed in Fig. 6.

The other important magnitude in the development of the vortical structures is the strain field, which is plotted in Fig. 16 for different phases of the forcing signal. The fields were obtained by applying Eq. (9) over the PIV data. Graph 16(a) shows the high-amplitude, three-structure case and graph 16(b) shows the low-amplitude, two-structure case.

The strain is substantial in three different zones. The zone in front of the nozzle exit should be eliminated, because the high strain values there only represent that over the nozzle wall the velocity is zero. The regions of considerable strain are:

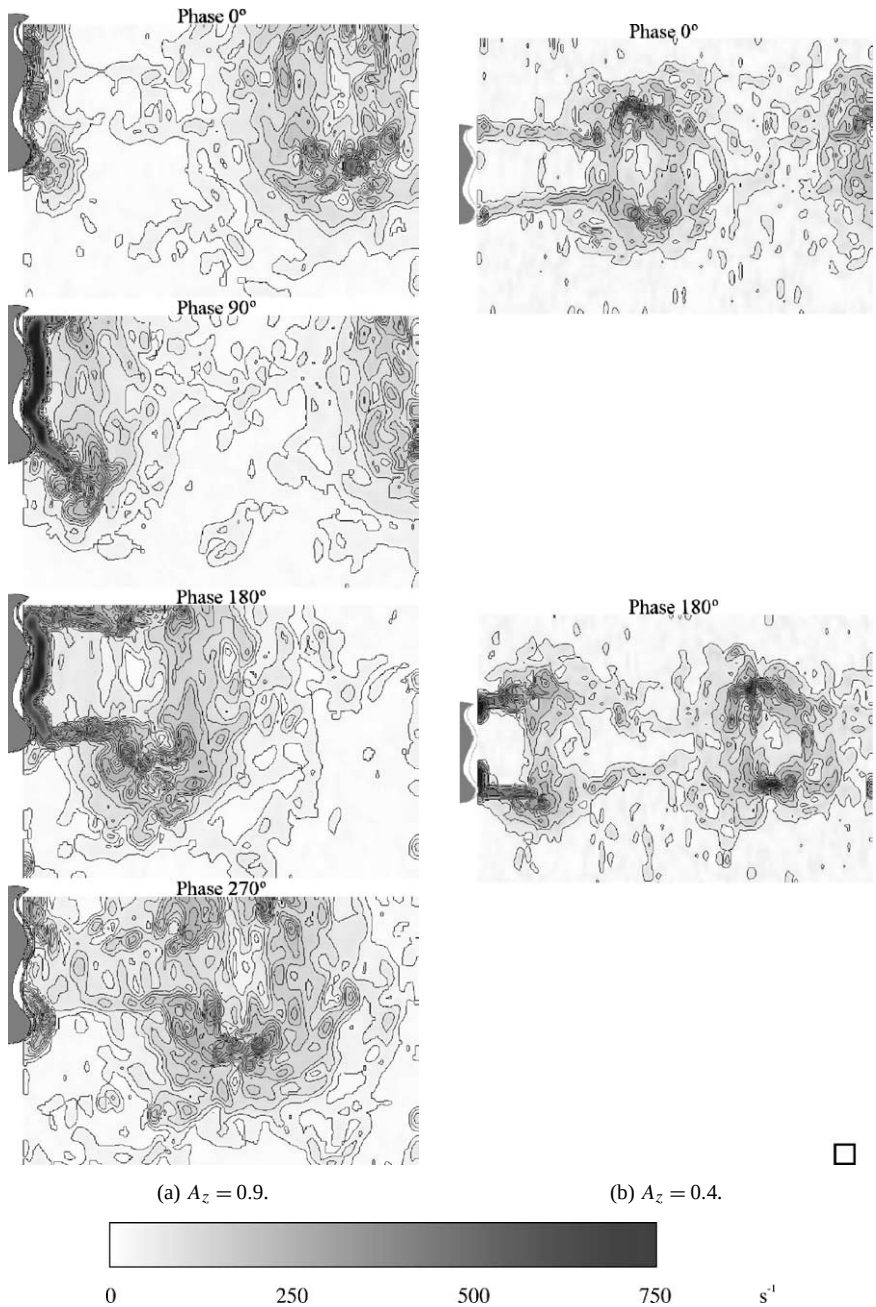

Fig. 16. Strain maps for equi-spaced phases along a forcing cycle. High (a) and low forcing (b) cases. The square in the lower right side represents the interrogation window size.

- The core of the azimuthal vortices (the strong primary vortices and the counter-rotating vortices).
- The shear layer in the vicinity of the nozzle exit, at a stage when the primary vortex has not been completely formed (has not completely detached from the nozzle exit).
- Around the primary ring, and also on its front and back (first on its front and then also on its back).

The behaviour described above is similar for the two configurations. This is consistent with the fact that the major difference between both configurations is the development of the third vortex structure, which has relatively small vorticity and do not add much to the deformation field main features.

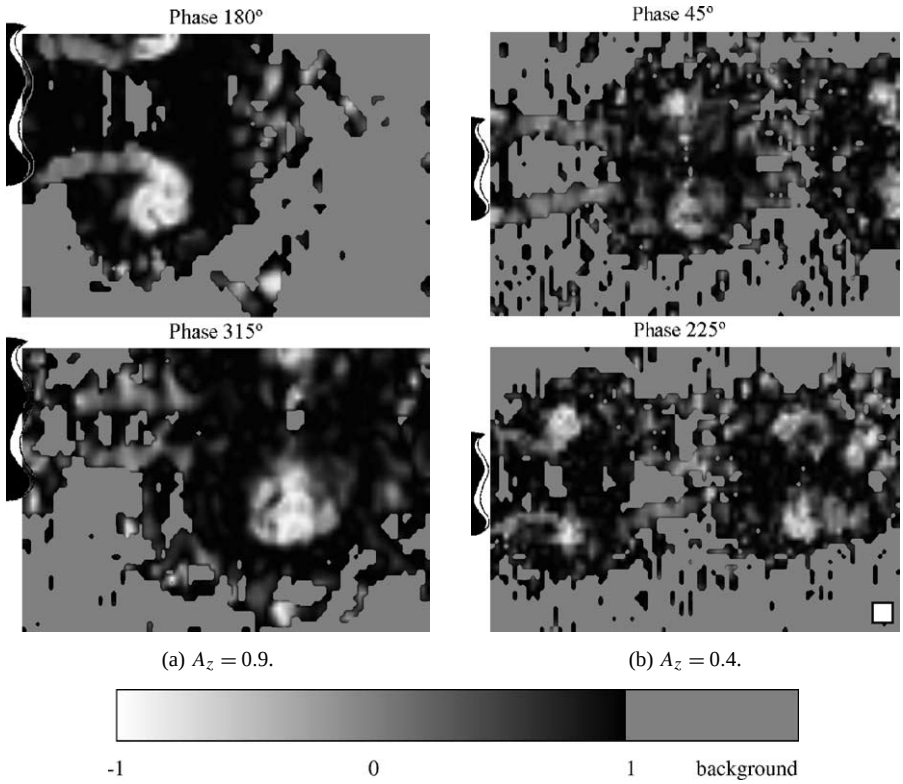

Fig. 17. Local parameter χ (defined in Eq. 10). High (a) and low forcing (b) cases. The square in the lower right side represents the interrogation window size.

The information on the strain field may be better understood if each local strain value is compared with the local vorticity. The squares of the magnitudes are used, as it is the vorticity modulus that is relevant for the comparison. Two parameters can be defined over the difference between squares (strain and vorticity): the actual difference and a normalised difference. The actual difference can be related with the pressure distribution as shown in Eq. (11); and the normalised difference is given by a local parameter, χ, as defined in Eq. (10). The parameter χ provides a sharp distinction between zones of dominant vorticity or dominant strain.

The local parameter is calculated by using Eq. (10) and it is plotted in Fig. 17 for two phases of the forcing signal. Graph 17(a) shows the high-amplitude, three-structure case and graph 17(b) shows the low-amplitude, two-structure case. The vorticity is dominant in the vortex cores (shown in light grey levels), while in their surroundings and in the braid region the strain is dominant and the zone is deforming (shown in dark grey levels). The parameter is zero in a subtle interface between the two regions and on the forming shear layer, which can be viewed as a vortex sheet (in (a) 180° and (b) 45°). The zones where both the strain and the azimuthal vorticity are small are shown in a medium grey level easy to difference from the other zones, as the information there is irrelevant and might be misleading.

An important rate of strain defined the region where the counter-rotating structure is supposed to develop for the high forcing case, based on visualisations and in the vorticity graphs. This high strain is a key feature, which has been supposed in the qualitative reasoning that lead to the sketches sown in Figs. 9 and 10.

The pressure distribution is shown in Fig. 18 for the same phases and configurations as the local parameter. If compared with the information in Fig. 17, it has to be taken into account that here, the Laplacian of pressure is not a dimensionless variable as the local parameter. Here, the difference between the vorticity and strain is shown in its actual magnitude. Therefore, the maps of pressure distribution show the major effect of the primary structure. The laplacian is only considerable (meaning appreciable pressure non-uniformities) in the vortex cores and in their surroundings. It is interesting to note that the initial shear layer coming from the nozzle lip shows a preponderance of the strain field, a fact that was overshadowed in the local parameter maps.

Finally, some information can be obtained about the azimuthal component of the velocity vector. The equations grouped in (12) allow obtaining an order of magnitude of the azimuthal velocities from the (u_r, u_z) velocity maps. The azimuthal velocity appears to be maximum in the vortex zone, and for azimuthal positions between valley and crest, where it will be

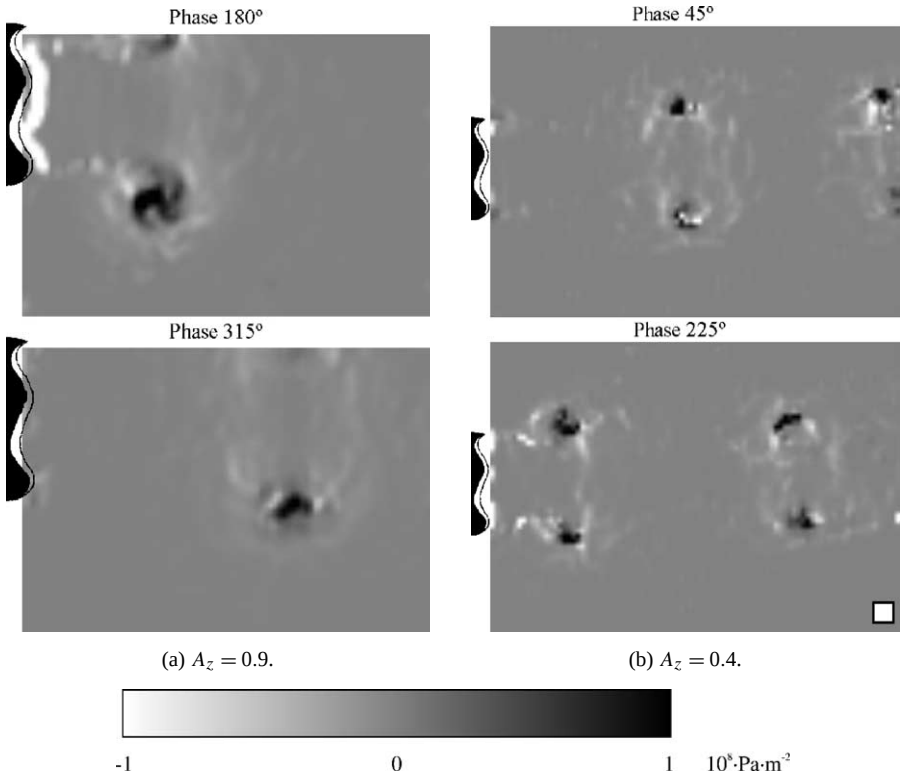

Fig. 18. Laplacian of the pressure (from Eq. 11). High (a) and low forcing (b) cases. The square in the lower right side represents the interrogation window size.

around 0.5 cm/s. A comparison of such value with those of the typical maximum radial and axial components in the zone (~ 0.5 m/s and ~ 1 m/s, respectively) shows that the flow can be considered two-dimensional, at least in the very near-field here considered.

6. Discussion

The first implication of this study is that the Reynolds number does not play a major role in the near-field dynamics of the forced co-flowing jet, thus validating the hypothesis of inviscid dynamics already used in [1]. This conclusion comes from the comparison between visualisations of two flows with Reynolds numbers varying roughly an order of magnitude (450, presented in [1], to 7000, presented in this work). The main features of the flow are equivalent in both flows, for the high forcing configurations presented in the previous work.

Another flow configuration, which was not considered in the previous experiments, is shown here, appearing for lower forcing amplitudes. This is a simpler configuration, where only the primary and secondary structures appear. In this case, the applied forcing acts in two ways. First, the forcing produces, in the very near field, developed concentrations of vorticity that form the primary structure. Therefore, a strain field of considerable strength exists very near to the nozzle lip. Second, as the counter-rotating structure does not concentrate, there is an increase on the amount of distributed azimuthal vorticity of opposite sign. Most authors [2,17] relate the origin of the secondary structure to the existence of residual distributed vorticity in the braids, and of a high strain, which enables it development. Thus, both effects lead to the concentration of a stronger secondary structure.

A close analysis of the quantitative results presented in this work serves to verify the suitability of the processes presented in Figs. 9 and 10. The concentrations of vorticity that are measured appear in the regions anticipated in [1], and they develop trajectories that are consistent with the inviscid vortex dynamics mechanisms commented there. Moreover, the information of the strain field supports the idea of a strong deformation of the counter-rotating vortex ring, which appear for high forcing conditions, as that vortex initially develops through a region of considerable strain. The derived variables obtained also support the enhanced development of the secondary structure for the low forcing case.

Due to its low spatial resolution, the information of derived fields from PIV data has too be considered with care. Artefacts of correlated noise, small-scale structures and effects like peak locking may affect the measurements. Hence, we have first performed a visualisation study and the PIV results have been obtained repetitively to avoid misleading information. Therefore, the structures and the vortex dynamics proposed have a solid foundation.

7. Conclusions

This paper presents an experimental study of the near field structure of co-flowing jets in which the inner jet is subjected to an axial forcing. As a result of it, the flow development changes considerably as compared to the unforced case, and lateral spreading configurations occur. These configurations are relevant for the jet entrainment. Two characteristic flow modes appear, depending on the forcing amplitude.

Different flow structures appear in the surroundings of the nozzle exit as concentrated vortices, due to the high axial forcing. Two of them are the well-known primary and secondary jet structures. Another structure of counter-rotating vortex rings may or not appear, being precisely this the reason of the existence of two distinct flow modes. For high forcing conditions, the counter-rotating vortex rings appear near the nozzle exit, interleaved with the array of vortex rings that conforms the primary structure. Due to their initial location and vorticity, these counter-rotating vortices strongly affect the flow evolution. For low forcing conditions, the counter-rotating rings do not concentrate and the flow evolution is controlled by the dynamic interactions of the two typical vortex structures.

The azimuthal vorticity maps obtained from the experimental PIV data validate the existence of the two azimuthal vortex structures (primary and counter-rotating). The strain fields provide additional evidence that permits to validate the hypothesis of a strong deformation of the two weaker structures. Therefore, the measurements corroborate the qualitative explanation of the flow development presented in [1] and here. An extension, or rather a simplification of the qualitative description, is performed, to elucidate the two-structure flow configuration.

The convective motion of the primary structure is also analysed. The convective velocity of the vortex rings is constant in the near field, after the vortex has detached from the nozzle exit lip. This velocity is directly proportional to the forcing amplitude. Therefore, the forcing amplitude directly affects the primary structure wavelength, a parameter of paramount importance because it controls the induction field of the most-energetic structure of the flow. A re-definition of the Strouhal number in these forced flows, taking account of this effect is customary for this reason.

Acknowledgements

The authors would like to thank Prof. Juan C. Lasheras for his important contribution at the initial stages of this work and Dr. Carlos Martínez-Bazán for useful comments and discussion.

References

[1] P. Rodríguez, U. Ruiz-Rivas, A. Lecuona, Near field vortex dynamics in axially forced, laminar, co-flowing jets: A descriptive study of the flow configurations, European J. Mech. B Fluids 20 (5) (2001) 673–698.
[2] S.J. Lin, G.M. Corcos, The mixing layer: Deterministic models of a turbulent flow. III. The effect of plane strain on the dynamics of streamwise vortices, J. Fluid Mech. 141 (1984) 139–178.
[3] R. Adrian, Particle-imaging techniques for experimental fluid mechanics, Annu. Rev. Fluid Mech. 23 (1991) 261–304.
[4] C. Willert, M. Gharib, Digital particle image velocimetry, Exp. Fluids 10 (1991) 181–193.
[5] E.J. Gutmark, F.F. Grinstein, Flow control with noncircular jets, Annu. Rev. Fluid Mech. 31 (1999) 239–272.
[6] U. Ruiz-Rivas, Vortex dynamics in the near field of a co-flowing jet subjected to axial forcing, PhD Thesis, Universidad Carlos III de Madrid, 2000.
[7] M. Raffel, C. Willert, J. Kompenhans, Particle Image Velocimetry, A Practical Guide, Springer-Verlag, 1998.
[8] O.A. Druzhinin, S.E. Elgobashi, Direct numerical simulation of a three-dimensional spatially developing bubble-laden mixing layer with two-way coupling, J. Fluid Mech. 429 (2001) 23–61.
[9] A.T. Hjelmfelt, L.F. Mockros, Motion of discrete particles in a turbulent flow, Appl. Sci. Res. 16 (1966) 146–161.
[10] H.T. Huang, H.E. Fiedler, J.J. Wang, Limitations and improvements of PIV. Part 1, Exp. Fluids 15 (1993) 168–174.
[11] J. Westerweel, Effect of sensor geometry on the performance of PIV Interrogation, in: Proc. 9th International Symposium on Applications of Laser Techniques to Fluid Mechanics, Lisbon, 1998.
[12] U. Ruiz-Rivas, A. Lecuona, P.A. Rodríguez, J.I. Nogueira, PIV Measurements in co-flowing jets subjected to axial forcing: Vorticity and strain field structure, in: Selected Papers 10th International Symposium on Applications of Laser Techniques to Fluid Mechanics, Lisbon 2000, Springer-Verlag, 2002.

[13] J. Nogueira, A. Lecuona, P. Rodríguez, Local field correction PIV, implemented by means of simple algorithms, and multigrid versions, Meas. Sci. Technol. 12 (2001) 1911–1921.
[14] R.L. Panton, Incompressible Flow, Wiley, 1984.
[15] P. Bradshaw, Y.M. Koh, A note on Poisson's equation for pressure in a turbulent flow, Phys. Fluids 24 (1981) 777.
[16] M. Tanaka, S. Kida, Characterization of vortex tubes and sheets, Phys. Fluids A 5 (9) (1993) 2079–2082.
[17] D. Liepmann, M. Gharib, The role of streamwise vorticity in the near field entrainment of a round jet, J. Fluid Mech. 245 (1992) 643–668.
[18] J.E. Martin, E. Meiburg, Numerical investigation of three-dimensionally evolving jets subject to axisymmetric and azimuthal perturbations, J. Fluid Mech. 230 (1991) 271–318.
[19] F. Grinstein, E. Gutmark, T. Parr, D. Hanson-Parr, U. Obeysekare, Streamwise and spanwise vortex interaction in an axisymmetric jet, Phys. Fluids 8 (1996) 1515–1524.
[20] P. Brancher, J.M. Chomaz, P. Huerre, Direct numerical simulations of round jets: Vortex induction and side jets, Phys. Fluids 6 (5) (1994) 1768–1774.
[21] M. Van Dyke, An Album of Fluid Motion, Parabolic Press, Stanford, 1982, The visualisations of Didden at which this article refers are plate 76.
[22] J.C. Lasheras, A. Liñan, A. Lecuona, P. Rodríguez, Vorticity dynamics in three-dimensional pulsating co-flowing jet diffusion flames, in: J. Jiménez (Ed.), The Global Geometry of Turbulence, 24th Symposium on Combustion, in: NATO ASI Series B, Vol. 268, 1992, pp. 325–332.